Heliyon 10 (2024) e38385

Contents lists available at ScienceDirect

Heliyon

journal homepage: www.cell.com/heliyon

Research article

Biomimetic siRNA nanogels for regulating macrophage polarization and promoting osteogenesis

Xianwen Ma [a,#], Qi Zhou [b,#], Zhaofeng Liu [b,#], Yibei Wang [b,*,1], Yong Hu [a,**,1]

[a] Department of Orthopedics, The First Affiliated Hospital of Anhui Medical University, Hefei 230022, Anhui Province, China
[b] Division of Orthopaedic Surgery, Department of Orthopaedics, Nanfang Hospital, Southern Medical University, Guangzhou, Guangdong, 510515, China

ARTICLE INFO

Keywords:
Bone fracture healing
Macrophage polarization
siRNA therapy
Biomimetic nanogels
Osteogenic differentiation

ABSTRACT

Background: Bone fracture regeneration poses significant clinical challenges due to complications such as delayed healing, nonunion, and the limitations of current treatments.
Objective: This study introduces a novel therapeutic approach utilizing biomimetic nanogels to silence the Ccl4 gene, aiming to promote bone repair by regulating macrophage polarization.
Methods: The nanogels, composed of tannic acid (TA) and small interfering RNA (siRNA), were designed for targeted gene delivery.
Results: In vitro findings indicate that siRNA-mediated Ccl4 reduction significantly improves M2 macrophage polarization, which, in turn, promotes osteogenic differentiation of bone marrow-derived mesenchymal stem cells. Increased expression of osteogenic markers and enhanced mineral deposition were observed. The nanogels demonstrated optimal particle size, stability, and cellular uptake, and biocompatibility assays confirmed their non-toxicity.
Conclusion: This study underscores the potential of targeted siRNA delivery in modulating immune responses to enhance bone regeneration, offering promising treatment options for complex bone healing scenarios.

1. Introduction

Bone fractures pose a substantial health and economic burden, with an increasing prevalence due to the aging global population [1–3]. Despite medical advancements, a significant subset of fractures heal poorly, leading to substantial patient distress and societal costs [4–6]. Traditional treatments, such as autologous bone grafts, are limited by material availability, and the use of bone morphogenetic proteins (BMPs) carries significant risks, including potential carcinogenic effects and inflammatory reactions [7–9]. The challenge lies in the development of a safe and effective treatment for difficult-to-heal fractures.

Effective bone healing is contingent upon the synergistic interplay between macrophages and BMSCs. Macrophage polarization, which is essential for BMSC differentiation, is a critical regulatory factor in this process. M1 macrophages initiate immune responses, while M2 macrophages facilitate tissue repair by promoting BMSC osteogenesis [10]. Recognized increasingly as crucial to bone

** Corresponding author.
* Corresponding author.
E-mail addresses: dr_wangyibei@163.com (Y. Wang), hyayfy08@126.com (Y. Hu).
# Contributed equally to this work.
1 contributed equally to this work.

https://doi.org/10.1016/j.heliyon.2024.e38385
Received 18 July 2024; Received in revised form 21 September 2024; Accepted 23 September 2024
Available online 24 September 2024

healing, M2 macrophages were the focus of this study, where we identified Ccl4 as a key gene influencing their polarization through RNA-seq analysis and in vitro experiments. Our study focused on M2 macrophages, which were identified as key to bone healing, and we targeted the Ccl4 gene, which influences their polarization, using RNA-seq and in vitro assays. siRNA holds significant therapeutic potential due to its ability to induce specific gene silencing [11–13]. Subsequently, we developed siRNA to modulate this gene, aiming to enhance BMSC osteogenic potential and improve bone healing.

Despite its advantages, siRNA's clinical application is hindered by delivery challenges, including susceptibility to degradation and cellular membrane impermeability [14,15]. To overcome these, we developed TA-siRNA nanogels, which protect siRNA from degradation. Known for its anti-inflammatory, antibacterial, and anticancer properties, TA has broad biomedical applications [16]. To facilitate targeted delivery, the application of mimicking RAW cell membranes which employ homologous targeting to specifically deliver drugs to enhance delivery efficiency and therapeutic outcomes in bone and joint disorders [17–19]. In this study, the physical and chemical properties of the nanogels, including particle size and stability, were characterized to ensure their suitability for siRNA delivery. In vitro biocompatibility assessments with BMSCs confirmed the nanogels' safety and effectiveness in cellular applications. Comprehensive analysis demonstrated the nanogels' ability to silence genes in macrophages, inducing a phenotype shift towards the M2 pro-healing state. This study marks the use of TA-siRNA nanogels for targeted gene delivery to improve bone fracture healing, providing a new strategy for the development of biomimetic materials for complex bone regeneration in regenerative medicine.

2. Methods and materials

2.1. Data acquisition, standardization, and analysis of gene expression Omnibus (GEO) data sets

Data sets relevant to bone fracture healing were systematically searched and selected from the GEO database. Specifically, two GEO datasets, GSE161315 and GSE53256, were chosen based on their relevance to the study. GSE161315 contains transcriptomic data comparing normal healing with delayed healing in Rattus norvegicus, while GSE53256 includes data comparing young and old rats. The raw data from both datasets were downloaded for further analysis.

The raw data were preprocessed and normalized using the Robust Multi-array Average (RMA) method to correct for any technical variations and to ensure consistency and comparability across samples. Box plots were generated to visualize the distribution of gene expression values across the samples and to identify any outliers.

Principal Component Analysis (PCA) was performed to reduce the dimensionality of the data and to identify potential clustering based on different experimental conditions. The PCA plots were generated to show the separation of samples into distinct groups: normal vs. delayed healing for GSE161315 and young vs. old for GSE53256. Differential expression analysis was conducted using the "limma" R package to identify genes with significant changes in expression between the different groups. The analysis provided a list of differentially expressed genes (DEGs) with corresponding statistical significance values. Volcano plots were used to visualize the upregulated and downregulated genes in each dataset.

Heatmaps were generated to visualize the expression patterns of the DEGs across the samples. The heatmaps illustrated distinct clustering of genes and samples, further supporting the results from the differential expression analysis. To understand the biological significance of the DEGs, Gene Ontology (GO) and Kyoto Encyclopedia of Genes and Genomes (KEGG) pathway enrichment analyses were performed. A Venn diagram was created to show the overlap of DEGs between the two datasets, indicating common and unique genes involved in the healing process. GO enrichment analysis revealed significant biological processes, while KEGG pathway analysis identified key signaling pathways involved in bone healing.

A Protein-Protein Interaction (PPI) network was constructed to identify key genes based on their connectivity and functional significance. Several central genes, including Ccl4, were highlighted as significant nodes within the network, as identified by different centrality measures such as MCC, DMNC, and MCODE clustering.

2.2. Isolation and characterization of BMSCs

BMSCs were harvested from the medullary cavities of both humeri and femurs of 2-week-old female SD rats. The BMSCs were subsequently cultured in low-glucose Dulbecco's Modified Eagle Medium (DMEM), enriched with 10 % fetal bovine serum (FBS; Gibco), and maintained at a temperature of 37 °C in an atmosphere containing 5 % CO_2.

2.3. Preparation of self-Assembled TA@SiCcl4 nanogels

To begin, prepare a solution of siRNA at a concentration of 0.2 O.D/mL and a TA solution at 0.2 w/v% using nuclease-free PBS. Place 1 mL of the siRNA solution in an ice bath and stir at 100 rpm for 3 min using a magnetic stirrer. Then, add 1 mL of the 0.2 w/v% TA solution dropwise to the siRNA solution and react for 30 min. Transfer the mixture to a 100 kDa centrifugal filter unit (Amicon Ultra-4 Ultracel-100 K, Millipore) and dialyze for 24 h to remove unreacted TA and siRNA. Afterwards, add 200 μL of nuclease-free PBS to the nanogel, and store the TA-siRNA nanogel stock solution at 4 °C.

2.4. Preparation of biomimetic nanovesicles MTA@SiCcl4

Cultivate Raw cells in vitro in large quantities, scrape them from the culture dish with a cell scraper, and resuspend in enzyme-free PBS to obtain a cell suspension. Add the cell suspension to a hypotonic lysis buffer containing protease inhibitors. Place the solution in

an ice bath for 15 min, then subject it to repeated freeze-thaw cycles in liquid nitrogen, and perform differential centrifugation to obtain the RAW cell membrane. Thoroughly mix the TA-siRNA nanogel solution with the cell membrane solution in a 1:1 mass ratio to produce MTA@SiCcl4. Sequentially extrude this solution through manual extruders with 400 nm and 200 nm porous polycarbonate membranes, respectively, to finally prepare the biomimetic nanovesicles MTA@SiCcl4. Store the collected gene-carrying biomimetic nanovesicles MTA@SiCcl4 in water at 4 °C for future use.

2.5. Characterization of self-Assembled TA-siRNA nanogels and biomimetic nanovesicles MTA@SiCcl4

The successful synthesis of TA-siRNA nanogels is confirmed by the Tyndall effect. To do this, prepare TA, siRNA, and TA-siRNA solutions and illuminate with infrared light; the appearance of the Tyndall effect indicates successful synthesis of the TA-siRNA nanogels. Examine the morphology of the nanogels using Transmission Electron Microscopy (TEM): drop the prepared solutions on a 200-mesh copper grid, allow to sit at room temperature for over 6 h to ensure evaporation of water, and observe with TEM. Measure the size distribution and zeta potential of the nanogels using a dynamic light scattering analyzer (Zetasizer Nano ZS, Malvern). Phagocytosis experiment: Seed RAW cells into a six-well plate, add medium, and culture for 6 h to allow cells to adhere. Under sterile conditions, prepare the original TA-siRNA nanogel solution and biomimetic nanovesicles MTA@siCcl4, labeling the TA-siRNA nanogels with FITC (green light) and Raw cell membranes with Dil (orange-red dye). Add TA-siRNA or MTA@SiCcl4 to the well plate, incubate in a culture incubator for 2 h, then observe cell phagocytosis with confocal laser microscopy.

2.6. In vitro stability and Bioactivity Testing

2.6.1. In vitro cytocompatibility analysis

In order to conduct in vitro cytocompatibility examination, the live/dead staining, proliferation test, and β-actin Staining Kit (Abkine) were employed to evaluate each sample. The survival of 5×10^5 RAW cells were evaluated using calcein-AM/ethidium (CalceinAM/PI, Invitrogen). Each sample was cultured on a 12-well plate one day later. The BMSCs were incubated for 20 min at 37 °C after being combined with a culture mixture containing 3 M Calcein-AM and 5 M PI. The quantification of RAW cells proliferation was conducted subsequent to their cultivation for durations of 1, 3, and 7 days in a 12-well plate supplemented with CCK-8 solution. A 100 μL/mL CCK-8 solution was added to 12-well coculture plates containing RAW cells and samples. The supernatant's optical density (OD) values were determined at 450 nm using a microplate analyzer (BioTech) after 2 h. The cytoskeleton of 2.5×10^5 BMSCs was examined by staining them with Actin-Tracker Green and Hoechst after a 3-day culture period in a 12-well plate. Microscopic images were acquired utilizing a confocal laser scanning microscope manufactured by Nikon.

2.6.2. The impact of Osteoimmunomodulation on osteogenic differentiation

For co-cultured assays, RAW cells were plated in the upper chamber of Transwell, while the lower chamber contained the BMSCs. A polycarbonate membrane with 1.0 mm pores was used to separate the two cell types, facilitating cytokine exchange between them. **2.6.3. Alkaline Phosphatase (ALP) Staining and Quantification.** The ALP staining kit (Beyotime) was used to stain BMSCs. After being fixed in 4 % paraformaldehyde for 30 min, the samples were stained with ALP dye according to the manufacturer's instructions. Following a duration of 1 h, every sample underwent three rounds of washing with distilled water to prevent discoloration. Subsequently, the outcomes were examined and captured utilizing an optical microscope manufactured by Olympus. An ALP Assay Kit (Beyotime) was employed to quantify BMSCs. Following a period of 7 days dedicated to the induction of differentiation, the medium was then disposed of, and the plate underwent a gentle rinsing process with PBS three times. Subsequently, the alkaline phosphatase activity of BMSCs was assessed in accordance with the guidelines provided by the ALP quantitative analysis kit. The ALP activity at a wavelength of 450 nm was evaluated using a microplate analyzer manufactured by BioTech.

2.6.3. The process of gene expression

The extraction of total RNA was performed using Trizol. Afterwards, it was converted into complementary DNA (cDNA) through reverse transcription using a reverse transcription kit (Takara). The experiment was carried out with the LightCycler 480II and the LightCycler 480 SYBR Green I Master apparatus manufactured by Roche. The experimental procedure was conducted in triplicate, and the quantitative analysis was performed using the $2^{-\Delta\Delta Ct}$ method.

2.6.4. Immunofluorescence and western bolt

Following a 30-min period of paraformaldehyde fixation, the cells were treated with PBS supplemented with 0.1 % TritonX-100 and 3 % BSA at ambient temperature. After a duration of 1 h, the suitable primary antibodies were introduced and left to incubate overnight at a temperature of 4 °C. Subsequently, the secondary antibodies were injected for a duration of 1 h. Micrographs were captured using a confocal reflection microscope (Leica) subsequent to the application of Hoechst dye to the nuclei (Sigma). The Western blot analysis was conducted. The cells were lysed on ice using the CWBIO lysis solution, which contained protease and phosphatase inhibitors (Thermo Fisher). The determination of protein concentrations was conducted utilizing a BCA protein assay kit. A protein slurry weighing 40 g was subjected to denaturation at a temperature of 100 °C for a duration of 10 min. The proteins were then separated using SDS-PAGE electrophoresis and subsequently deposited onto polyvinylidene fluoride membranes (PVDF, Thermo Fisher). Following a 1-h period of immersion in 5 % skimmed milk, the membranes were subjected to overnight incubation with the primary antibodies at a temperature of 4 °C. Immunoblots were seen using an enhanced chemiluminescence (ECL) kit after 1 h of incubation with secondary antibodies (CST). The protein density was quantified using the ImageJ program.

3. Results

3.1. Data Retrieval, extraction, and analysis of GEO data sets

The raw data for GSE161315 and GSE53256 were successfully downloaded and normalized using the RMA method. Box plots (Fig. 1A) showed consistent distribution of gene expression values across the samples, indicating effective standardization. PCA plots (Fig. 1B) revealed clear separation between normal and delayed healing groups in GSE161315 and between young and old groups in GSE53256, indicating distinct gene expression profiles. The differential expression analysis identified 142 DEGs in GSE161315 (85 upregulated and 57 downregulated) and 168 DEGs in GSE53256 (96 upregulated and 72 downregulated). Volcano plots (Fig. 1C) illustrated these changes in gene expression.

Heatmaps (Fig. 1D) demonstrated distinct clustering of DEGs, with clear differentiation between the experimental groups, supporting the validity of the differential expression results. The Venn diagram (Fig. 2A) showed 63 overlapping DEGs between the two datasets. GO enrichment analysis (Fig. 2B) highlighted processes such as cytokine-mediated signaling and cell chemotaxis. KEGG pathway analysis (Fig. 2C) identified pathways like cytokine-cytokine receptor interaction and NF-kappa B signaling, which are critical for bone healing. The PPI network analysis identified several key genes, with Ccl4 being prominently featured across different centrality measures (Fig. 2D, E, and 2F).

This underscores the importance of Ccl4 in the regulatory network, suggesting its potential role in enhancing macrophage polarization and promoting bone healing. By integrating PCA, differential expression, enrichment analyses, and PPI network construction, we identified Ccl4 as a crucial gene involved in the bone healing process, providing a foundation for potential therapeutic strategies targeting macrophage polarization.

3.2. Material characterization

As shown in Fig. 3A and B, neither the TA solution nor the siCcl4 solution exhibits the Tyndall effect, which can be attributed to the uniform dispersion of molecules within the solutions. In contrast, the TA@siCcl4 solution displays the Tyndall phenomenon due to the self-assembly of TA and siCcl4 into nanoparticles, which scatter light and thus cause this effect. Fig. 3C indicates that the TA-siRNA nanogels range in size from 100 to 150 nm, and compared to the TA@siCcl4 nanogels, the cell membrane-wrapped MTA@siCcl4 exhibits a distinct core-shell structure. Furthermore, the laser confocal colocalization image in Fig. 3D confirms the successful preparation of the biomimetic nanovesicles MTA@siCcl4. Electrophoretic light scattering assays show that the zeta potentials of TA@SiCcl4 and MTA@SiCcl4 nanogels are -34.02 ± 6.43 mV and -31.12 ± 3.12 mV, respectively (Fig. 3E). These measurements indicate the colloidal stability of the nanogels, with both types displaying potentials that suggest moderate stability, although MTA@siCcl4 shows a slightly less negative potential. Fig. 3F demonstrates that compared to TA@siCcl4, MTA@siCcl4 is more effectively engulfed by RAW264.7 cells within the same timeframe, indicating its superior cell-targeting capability. Fig. 3G shows no significant change in the particle size of MTA@siCcl4 and TA@siCcl4.

These findings collectively contribute to the understanding of the physicochemical properties and cellular interactions of the synthesized nanogels, which are crucial for their potential applications in drug delivery and biomedical research.

3.3. In vitro biocompatibility of MTA@SiCcl4 nanocomplexes

The evaluation of biocompatibility for novel biomaterials is crucial for their application in regenerative medicine. This study extensively examined the interactions between TA-siRNA nanocomplexes and MTA@SiCcl4 biomimetic nanovesicles with RAW264.7 macrophages to assess their suitability. Live/dead staining indicated that macrophage viability exceeded 95 % across all experimental conditions, as corroborated by quantitative analysis (Fig. 4A–C). These results suggest that the biomaterials are non-toxic and compatible with macrophages. Morphological analysis through actin staining demonstrated significant cellular adhesion and spreading on the surfaces of these biomaterials, indicating active cellular processes (Fig. 4B). This was quantitatively confirmed by measuring the cell spread area, illustrating that the materials support cellular attachment and spreading (Fig. 4D). Moreover, the CCK-8 assay revealed effective proliferation of BMSCs in the presence of these materials over a seven-day period, confirming that cellular growth and function remain intact (Fig. 4E). The consistent results across all groups underscore the potential of these biomaterials for bone tissue engineering. Statistical analysis showed no significant differences among the groups, reinforcing the materials' suitability for further in vivo studies.

The findings support the potential integration of these nanocomplexes and vesicles in bone regeneration therapies, offering a compatible interface for cellular growth and function.

3.4. RAW264.7 cells Respond to inflammation

MTA@SiCcl4 enhances macrophage phenotypic reprogramming in vitro. To determine the impact of MTA@SiCcl4 on macrophage polarization, RAW264.7 cells were incubated with PBS, siCcl4, TA@SiCcl4, and MTA@SiCcl4. The markers indicative of M1 (iNOS) and M2 (Arg-1) macrophage phenotypes were identified through immunofluorescence staining. Fig. 5A illustrates a pronounced shift in RAW264.7 cells treated with MTA@SiCcl4 towards the M2 phenotype from the M1 state. The use of MTA@SiCcl4 treatment led to a notable 1.8-fold drop in iNOS expression, which indicates M1 polarization. Additionally, there was a rise in Arg-1 expression by roughly 2.3-fold, showing a reduction in the M2 pro-inflammatory condition. To delve deeper into the influence of MTA@SiCcl4 on

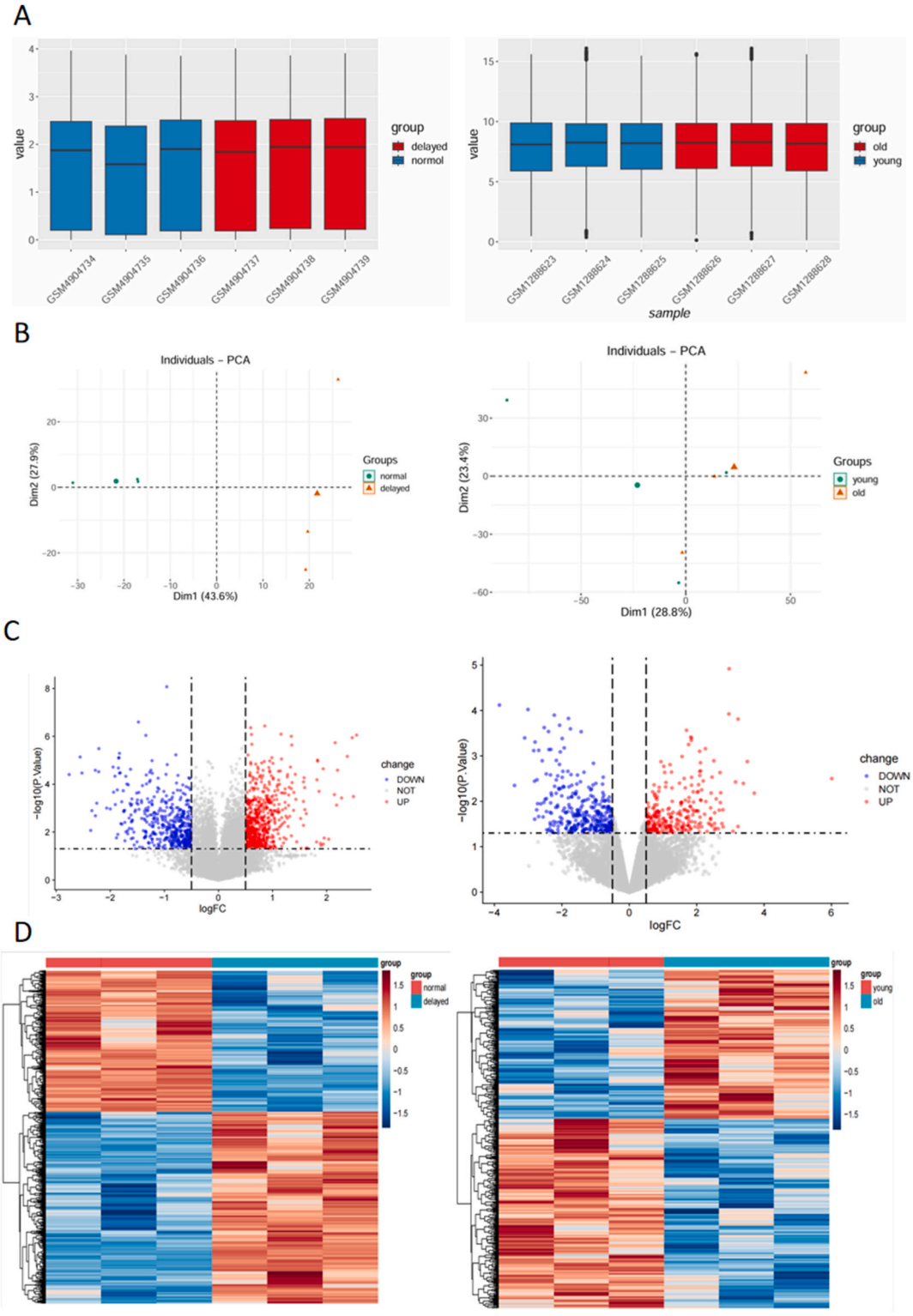

(caption on next page)

Fig. 1. Comprehensive Gene Expression and Interaction Analysis Post-Batch Effect Correction. (A) Boxplot illustrating the gene expression data after batch effect correction from datasets GSE161315 and GSE53256. (B) Principal Component Analysis (PCA) scatter plots showing the distribution of individuals and the separation between groups post-correction; 'normal' and 'delayed' in one, and 'young' and 'old' in the other, indicating variability and clustering within the datasets. (C) Volcano plots representing differential analysis between the two datasets, highlighting genes with significant expression changes: up-regulated (red), down-regulated (blue), and non-significant (gray). (D) Heatmaps displaying the expression patterns of differentially expressed genes across the two datasets, revealing distinct gene expression profiles between the compared groups.

macrophage polarization, the transcriptional levels of genes associated with M1 polarization, including iNOS, IL-6, and TNF-α, and those with M2 polarization, including IL-10 and Arg-1, were examined using reverse transcription RT-qPCR, as depicted in Fig. 5D and E. RT-qPCR confirmed these alterations, revealing a 55 % decrease in iNOS mRNA levels and a 120 % increase in Arg-1 mRNA levels. In comparison to the control group, the pro-inflammatory cytokines IL-6 and TNF-alpha were substantially reduced by 55 % and 60 %, respectively, in the groups treated with MTA@SiCcl4, demonstrating the anti-inflammatory properties of the nanovesicles. In contrast, the levels of the anti-inflammatory cytokine IL-10 increased by 120 %, further supporting the transition towards a healing-promoting M2 phenotype. Furthermore, there was a significant drop in the expression of the Ccl4 gene, with a 70 % reduction compared to the control group. This confirms that the siRNA-mediated silencing within the nanocomplexes was successful. This decrease verifies siRNA transport and functional activity and suggests that MTA@SiCcl4 nanovesicles may alter macrophage behavior toward a regenerative phenotype.

These findings demonstrate that MTA@SiCcl4 nanovesicles not only promote macrophage polarization towards an M2 phenotype but also effectively modulate the inflammatory gene expression profile in RAW264.7 cells, including the targeted silencing of Ccl4. This modification in the function of macrophages is essential for diminishing inflammation and creating a favorable environment for bone regeneration. The capacity to manipulate the phenotype of macrophages through targeted administration of siRNA demonstrates a promising approach to enhance the effectiveness of regenerative medicine in the treatment of complicated bone fractures.

3.5. Activation of M2-Polarized macrophages promote BMSCs differentiation

BMSCs play a crucial role in bone regeneration, primarily through their differentiation into osteoblasts, essential for effective bone repair. The interaction between BMSCs and their microenvironment, especially with immune cells such as macrophages [20], significantly influences BMSC fate. This study builds on recent insights that M2-polarized macrophages foster an osteogenic environment20, assessing the impact of M2-polarized RAW264.7 cells on the differentiation of BMSCs in a co-culture system. M2 macrophages were co-cultured with BMSCs under osteogenic conditions. Osteogenic differentiation was evaluated using several markers, including the enzymatic activity of ALP, and the expression of osteogenic markers such as RunX2 and osteopontin (OPN). Seven days post-co-culture, ALP activity was quantitatively analyzed, showing significantly elevated levels in BMSCs co-cultured with M2 macrophages compared to controls (Fig. 6A and B). Immunofluorescent staining was conducted seven days post-co-culture, revealing substantial increases in RunX2 and OPN, indicative of enhanced osteoblastic differentiation (Fig. 6C and D). Western blot analysis further corroborated these findings, indicating increased protein levels of RunX2 and OPN after seven days (Fig. 6E and F). These findings were supported by RT-qPCR, which showed elevated mRNA levels for collagen type I, RunX2, and OPN, suggesting transcriptional regulation as a mechanism for enhanced differentiation (Fig. 6G).

The consistent results across different markers underscore the potential of M2-polarized macrophages to significantly enhance outcomes in bone tissue engineering. The observed upregulation of osteogenic markers provides compelling evidence of the therapeutic potential of M2-polarized macrophages in bone regeneration. This approach may pave new pathways for regenerative therapies that utilize the interplay between the immune system and stem cells for efficient and effective bone repair.

4. Discussion

Our study explored the impact of MTA@SiCcl4 nanovesicles on macrophage polarization and subsequent bone regeneration, integrating extensive gene expression analyses, nanomaterial characterization, and detailed assessments of cellular responses. Material characterization confirmed the effective nanoparticle formation and stability of TA@siRSOP2 and MTA@siRSOP2 nanogels, with a consistent size range of 100–150 nm suitable for biological applications and a core-shell structure essential for their function as delivery vehicles. The colloidal stability, indicated by the Tyndall effect and appropriate zeta potential values, is critical for the biological functionality of these nanovesicles.

In terms of biocompatibility and cellular response, the nanovesicles exhibited high viability in macrophage cultures, maintaining over 95 % cell viability and promoting cellular adhesion and proliferation. This underscores their potential for in vivo applications in tissue engineering. Moreover, the treatment with MTA@SiCcl4 nanovesicles resulted in a significant shift in macrophage behavior, reprogramming RAW264.7 cells from a pro-inflammatory M1 phenotype to a regenerative M2 phenotype. This transition was marked by notable changes in gene expression, including a decrease in pro-inflammatory markers and an increase in anti-inflammatory and regenerative markers.

The enhanced osteogenic differentiation of BMSCs co-cultured with M2-polarized macrophages underscores the effectiveness of MTA@SiCcl4 nanovesicles in fostering a microenvironment conducive to bone regeneration. The upregulation of critical osteogenic markers such as ALP, RunX2, and osteopontin, following co-culture with M2 macrophages, indicates a significant enhancement in bone matrix formation and mineralization, crucial for successful bone repair.

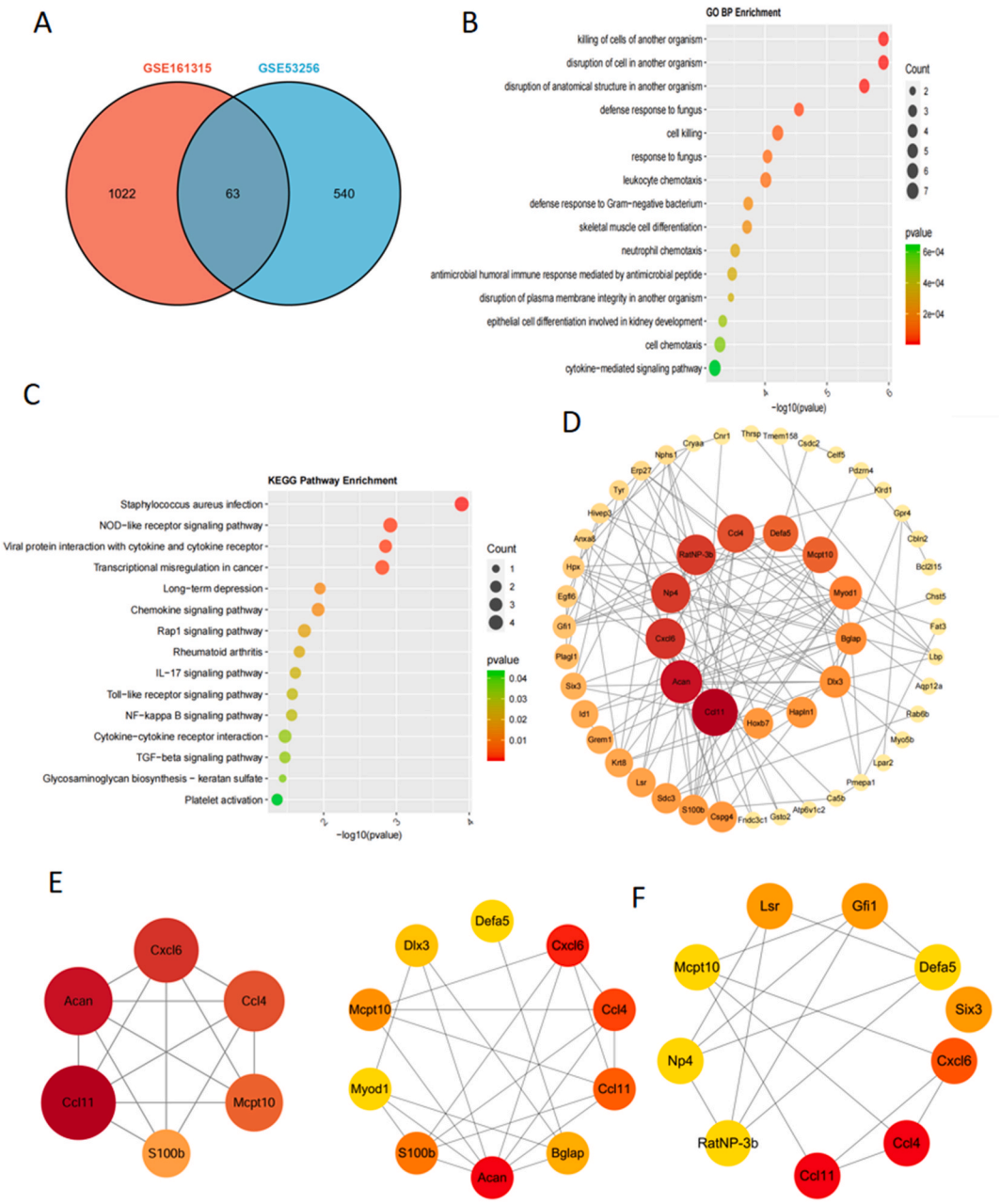

Fig. 2. Pathway Enrichment and Protein-Protein Interaction Network Analysis. (A) Venn diagram showing the overlap of differentially expressed genes between datasets GSE161315 and GSE53256. (B) GO enrichment analysis bubble chart, visualizing enriched biological processes with a color gradient representing p-value significance and bubble size denoting gene count. (C) KEGG pathway enrichment analysis bubble chart, displaying enriched pathways with the same visualization strategy as GO analysis. (D) PPI network generated using the Local Association Centrality (LAC) algorithm in CytoNCA, emphasizing the interconnectedness among the intersection genes. (E) The highest-scoring cluster module identified from the PPI network of all intersection genes using the MCODE algorithm, highlighting key gene interactions. (F) The top 10 pivotal genes ascertained by the MCC and DMNC topological analysis algorithms, indicating potential core genes in the network.

Our research extends the current scientific frameworks by elucidating the complex interactions between siRNA-mediated interventions and macrophage functionality within the bone regeneration context. By leveraging MTA@SiCcl4 nanovesicles to modify macrophage behavior, we elucidate a vital mechanism wherein localized gene silencing significantly impacts tissue repair and regeneration outcomes. Notably, siRNA targeting the Ccl4 gene markedly reduces its expression in macrophages, facilitating a shift from a pro-inflammatory (M1) to a regenerative (M2) phenotype. This shift is critical as M2 macrophages play a key role in reducing inflammation and promoting healing, aligning with a growing body of evidence that supports macrophage phenotype manipulation as

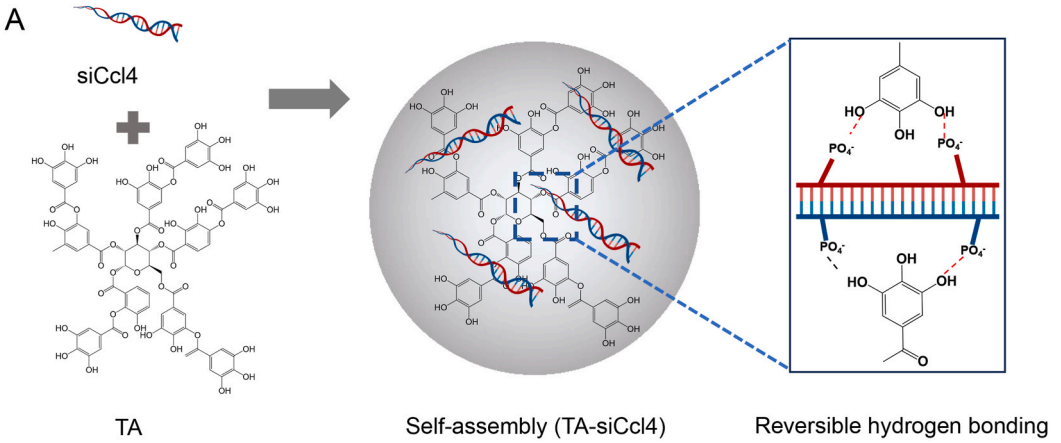

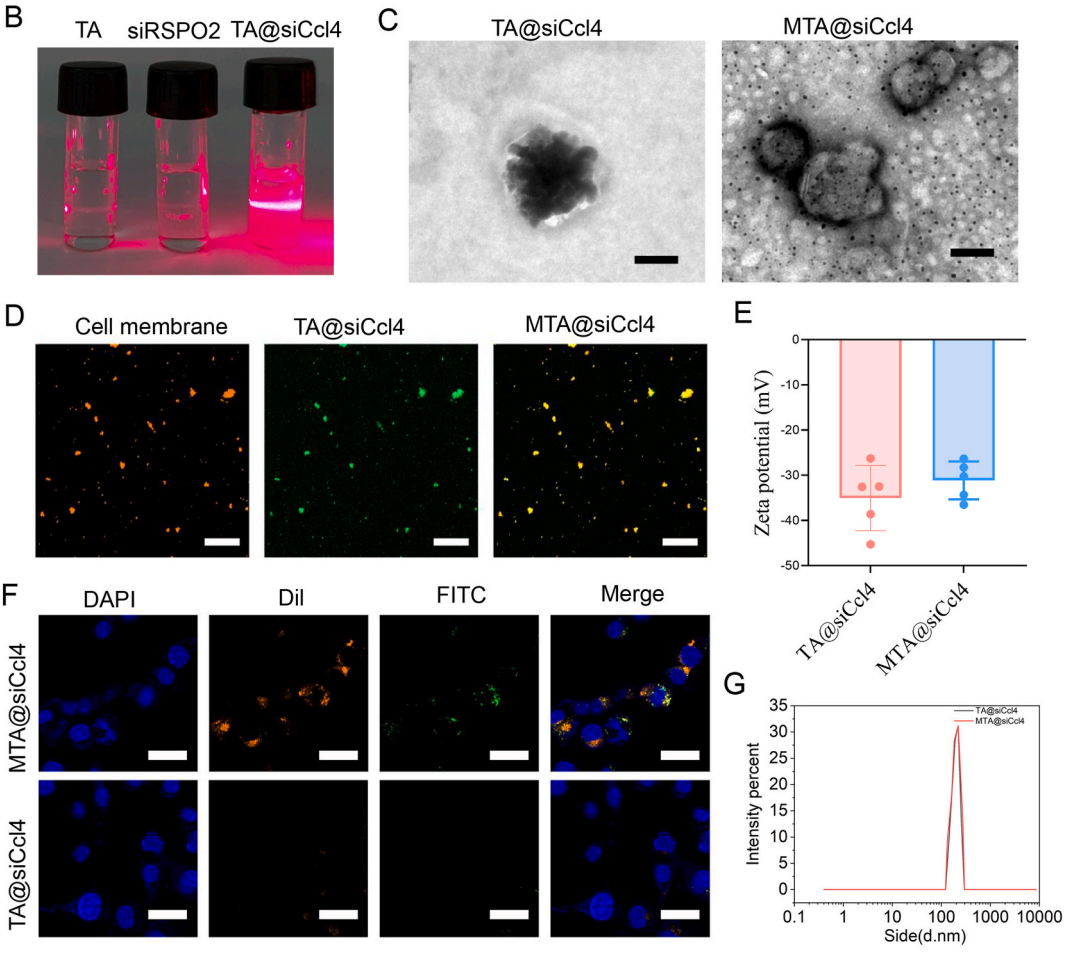

(caption on next page)

Fig. 3. Characteristics of TA-siRNA Nanocomplexes and Biomimetic Nanovesicles MTA@SiCcl4. (A) Schematic diagram of synthesis of TA-siRNA nanogel. (B) The Tyndall effect confirms the synthesis of TA-siRNA, indicated by the light scattering in TA-siRNA solutions, unlike the homogeneous TA and siRNA solutions. (C) Size range and core-shell morphology of the TA-siRNA and MTA@SiCcl4 are visualized via TEM, with a notable core-shell structure evident for the biomimetic vesicles (Scale bar = 100 nm). (D) The successful formulation of biomimetic nanovesicles MTA@SiCcl4 is corroborated by confocal co-localization imaging, denoting proper assembly (Scale bar = 1 μm). (E) Particle size analysis shows an average zeta potential of −35.32 ± 8.32 for TA@SiCcl4 and -46.32 ± 9.16 for MTA@SiCcl4. (F) Phagocytosis assay results highlight enhanced uptake of MTA@SiCcl4 by Raw 264.7 cells over TA@SiCcl4, suggesting superior cell-targeting capability (Scale bar = 20 μm). (G) Stability tests reveal no significant change in particle size for both MTA@SiCcl4 and TA@SiCcl4, indicating robust stability. Figures presented as Portable Network Graphics (PNG) with true color at 24 bits per pixel and dimensions of 1096x986 pixels, interlaced for optimal web display.

a therapeutic strategy to enhance regenerative processes [21].

Furthermore, the therapeutic potential of siRNA in bone regeneration is affirmed by its capability to precisely adjust the molecular environment at the bone repair site, promoting an anabolic state favorable for bone growth and remodeling. Our findings are consistent with recent research highlighting siRNA as a powerful and adaptable tool for manipulating key pathways in osteogenesis and bone homeostasis [22]. These insights are crucial, as they validate the use of siRNA for immune modulation and pave the way for novel RNA interference-based therapeutic strategies tailored for complex orthopedic conditions [23].

Effective bone regeneration requires complex interactions among various cell types, including osteoblasts, osteoclasts, and macrophages. Macrophages, in particular, play a pivotal role in this process due to their ability to adopt different phenotypes that influence healing stages. Traditionally, macrophages transition from a pro-inflammatory M1 phenotype, which aids in clearing debris and pathogens, to an anti-inflammatory and pro-healing M2 state that supports bone repair [24]. This phenotypic flexibility allows macrophages to adapt rapidly to environmental changes. In this study, we present initial evidence suggesting that silencing the Ccl4 gene promotes M2 polarization, potentially enhancing the osteogenic process. Our data preliminarily suggest that Ccl4 silencing might facilitate a shift towards an M2 phenotype, which is known to secrete cytokines and growth factors that stimulate osteoblast activity and matrix formation [11].

The results of our study reveal a new feature of CCL4's function in macrophage biology. Specifically, we show that suppressing CCL4 leads to the promotion of M2 macrophage polarization, which in turn enhances bone regeneration. This observation contradicts previously established functions of CCL4, specifically its role in promoting the movement of preosteoclasts and its contribution to the formation of osteoclasts, as proposed by Lee et al. [25] in their study on the interactions between CCL4 and CCR5.The disparity between our findings and prior research could be ascribed to the intricate nature of CCL4's involvement in immune modulation. Although Lee et al. [25] highlighted CCL4's capacity to enhance preosteoclast cell migration via its receptor CCR5, contributing to osteoclast differentiation and bone resorption, our study indicates that in a different context, where macrophages are targeted for gene silencing, CCL4 can promote a reparative, anti-inflammatory macrophage phenotype. This shift in function underscores the versatile roles that immune mediators can play in different biological contexts.

Moreover, the modulation of CCL4 expression might provide a valuable therapeutic tool to balance bone resorption and formation, particularly in diseases characterized by excessive inflammatory responses or bone degeneration. The use of CCL4 silencing to promote M2 macrophage polarization offers a promising avenue for enhancing bone healing, suggesting that manipulating CCL4 could mitigate conditions such as osteoporosis and rheumatoid arthritis by promoting bone regeneration and reducing inflammation.

To create biomimetic nanovesicles MTA@SiCcl4, we next covered the outer layer of the nanogels with RAW264.7 cell membranes. The purpose of this process is to preserve the medicine from degradation and enable targeted drug administration. TA is a naturally occurring polyphenol that is derived from gallic acid and has amphiphilic properties. The structure of this substance includes several galloyl groups, which have the ability to interact with a diverse array of organic, inorganic, hydrophilic, and hydrophobic materials through hydrogen bonding, electrostatic interactions, coordination bonds, and hydrophobic interactions. Tannic acid, known for its natural crosslinking properties and its ability to reduce inflammation, fight bacteria, and inhibit cancer growth, has been extensively researched for its potential uses in the field of biomedicine [16].

The material's surface consists of vesicles originating from Raw cell membranes, employing a homologous targeting strategy to accomplish precise drug delivery to osteoclasts. Homologous targeting exploits the distinctive characteristics of biomimetic vesicles, which are designed to imitate the cell membranes of particular cell types, such as RAW cells in the context of bone-related treatments. These vesicles have the ability to selectively target and adhere to cells that possess comparable traits, therefore enabling the direct delivery of therapeutic medicines to the precise location of injury or disease. Studies have demonstrated that this focused strategy enhances the effectiveness of treatment and improves the results in many experimental models of bone and joint disorders [17,18]. The objective of this study is to overcome the drawbacks of existing bone fracture treatments by utilizing the distinctive characteristics of TA-siRNA nanogels and homologous targeting mechanisms. This has the potential to benefit patients with fractures caused by osteoporosis due to various reasons (such as medication factors) [26].

5. Conclusion

In conclusion, our study not only advances our understanding of the role of Ccl4 in bone healing but also introduces a novel therapeutic modality using MTA@SiCcl4 nanovesicles for targeted gene silencing. The potential to modulate immune responses and enhance regenerative outcomes through such targeted interventions opens new avenues for the development of advanced therapeutic strategies in bone fracture healing and other regenerative medicine applications.

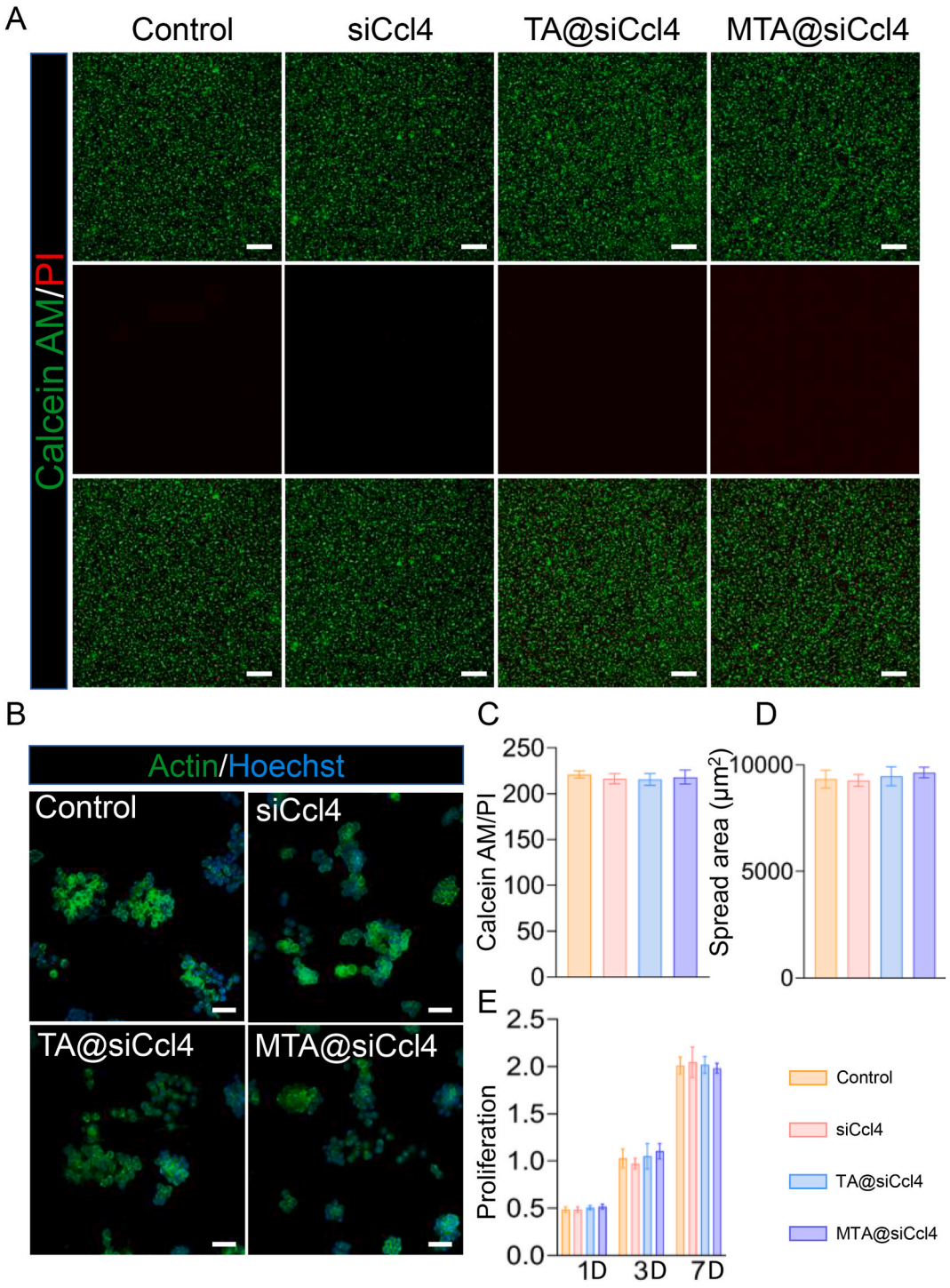

Fig. 4. Biocompatibility of each group. (A) Representative live/dead staining photos for RAW after contacting with siRNA, MTA@siCcl4 for 1 day. Red staining indicates dead cells, and green staining indicates live cells. Scale bar represents 200 μm. (B)The cytoskeleton images show the adhesion of RAW cultured on each sample after 3 days following culture. Scale bar represents 100 μm. (C)Quantitative analysis of live cells (n = 9). (D) Quantitative analysis of cell spread area (n = 9). (E)The CCK-8 assay was measured in each group after 1, 3, and 7 days of BMSCs culture (n = 5). ANOVA followed by Bonferroni's multiple comparison test was used for statistical analysis (*$p < 0.05$, **$p < 0.01$, ***$p < 0.001$).

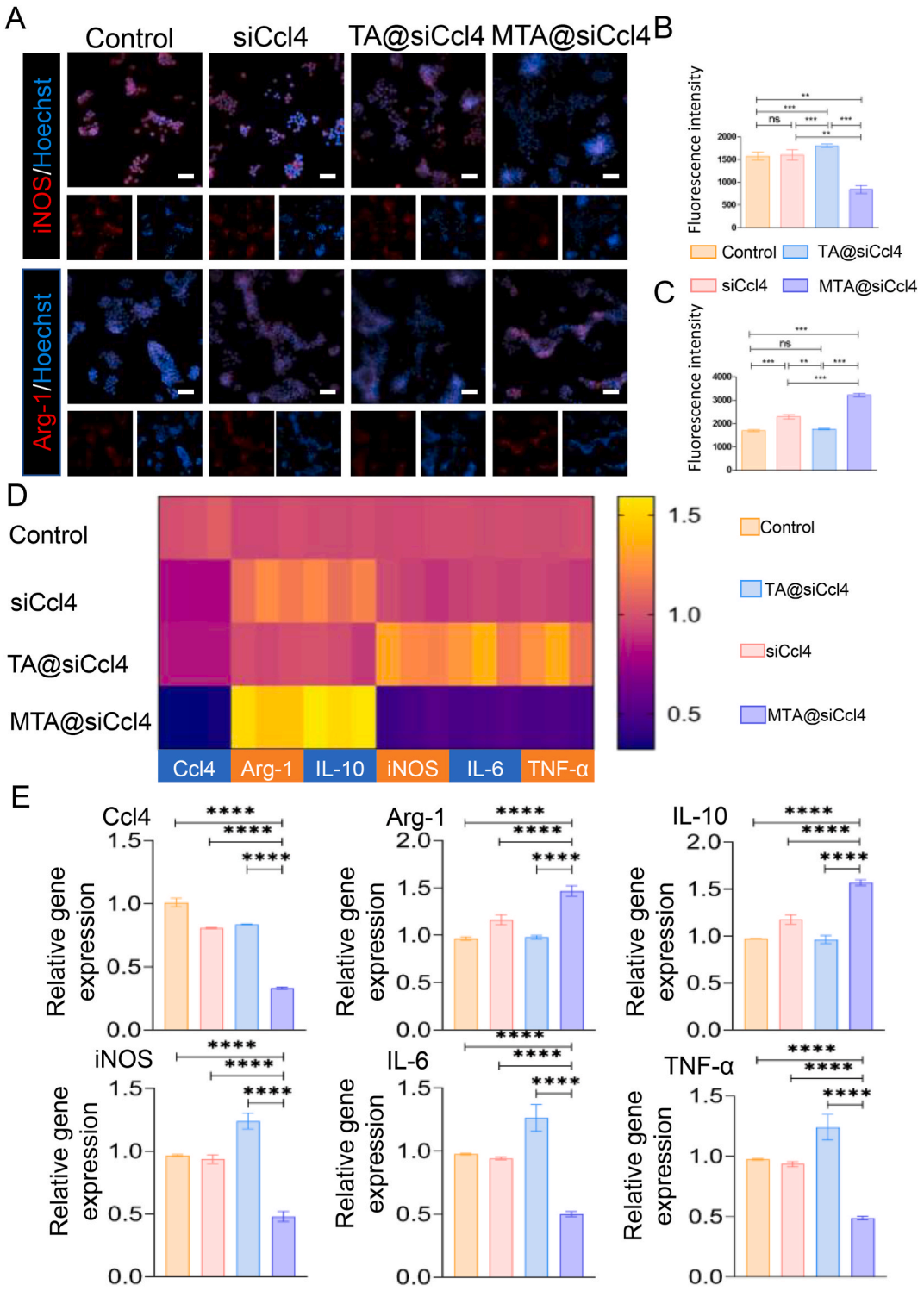

Fig. 5. In vitro RAW264.7 cell polarization. (A) Arg-1 and iNOS(red) immunofluorescent staining of RAW264.7 cells on each group surface 3 days after culture. Scale bar represents 50 μm. (B, C)) Quantitative analysis of the fluorescence intensity of iNOS and Arg-1 in each group (n = 3). (D, E) RT-qPCR was used to evaluate the effects of each group on the expression of inflammatory genes (n = 3). ANOVA followed by Bonferroni's multiple comparison test was used for statistical analysis (*p < 0.05, **p < 0.01, ***p < 0.001).

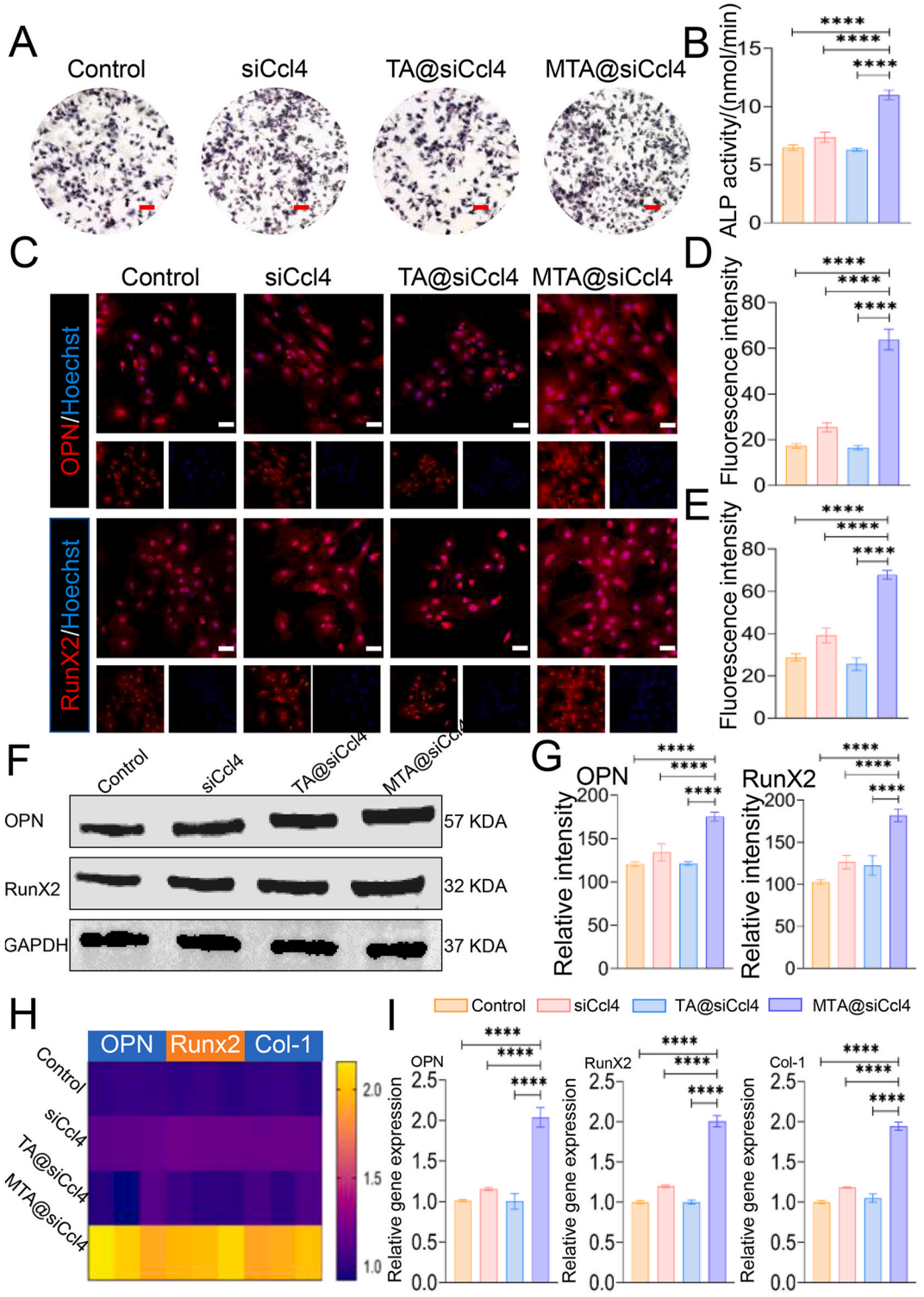

Fig. 6. Macrophage polarization effect on BMSCs osteogenesis. (A)ALP staining of BMSCs cultivated in a coculture system for 7 days. Scale bar represents 200 μm (B) Quantitative analysis of ALP staining (n = 5). (C) BMSCs were immunofluorescently stained with RunX2 and OPN 7 days after being cocultured. Scale bar represents 50 μm. (D, E) Quantitative analysis of immunofluorescent staining (n = 3).(F) Western blot analysis was used to assess RunX2 and OPN protein expression after 7 days. (G) Quantitative analysis of Western blot (n = 3). (H, I) After BMSCs were cocultured for 7 days (n = 3), RT-qPCR was used to evaluate theosteogenesis, including COL-1, RunX2 and OPN.ANOVA followed by Bonferroni's multiple comparison test was used for statistical analysis (*p < 0.05, **p < 0.01, ***p < 0.001).

CRediT authorship contribution statement

Xianwen Ma: Writing – original draft, Methodology, Investigation, Conceptualization. **Qi Zhou:** Writing – review & editing, Visualization, Validation, Formal analysis, Data curation. **Zhaofeng Liu:** Writing – review & editing, Supervision, Software, Resources. **Yibei Wang:** Writing – review & editing, Supervision, Conceptualization. **Yong Hu:** Writing – review & editing, Project administration, Funding acquisition.

Declaration of generative AI and AI-assisted technologies in the writing process

During the preparation of this work the authors used Claude in order to improve readability and language. After using this tool, the authors reviewed and edited the content as needed and take full responsibility for the content of the publication.

Declaration of competing interest

The authors declare the following financial interests/personal relationships which may be considered as potential competing interests: Yong Hu reports financial support was provided by Anhui Provincial Institute of Translational Medicine. Yong Hu reports financial support was provided by Anhui Medical University. If there are other authors, they declare that they have no known competing financial interests or personal relationships that could have appeared to influence the work reported in this paper.

Acknowledgement

We would like to thank the Research Fund of Anhui Institute of Translational Medicine (Grant Number: 2022zhyx-C34) for supporting this study. Additionally, we acknowledge the Program for Upgrading Basic and Clinical Collaborative Research of Anhui Medical University (Grant Number: 2023xkjT031) for their funding and support.

References

[1] regional Global, National burden of bone fractures in 204 countries and territories, 1990-2019: a systematic analysis from the Global Burden of Disease Study 2019, lancet Heal Longev. 2 (2021) e580–e592.
[2] S. Polinder, J. Haagsma, M. Panneman, A. Scholten, M. Brugmans, E. Van Beeck, The economic burden of injury: health care and productivity costs of injuries in The Netherlands, Accid. Anal. Prev. 93 (2016) 92–100.
[3] S. Singaram, M. Naidoo, The physical, psychological and social impact of long bone fractures on adults: a review, African J Prim Heal care Fam Med 11 (2019) e1–e9.
[4] M. Panteli, J.S.H. Vun, I. Pountos, A. J Howard, E. Jones, P.V. Giannoudis, Biological and molecular profile of fracture non-union tissue: a systematic review and an update on current insights, J. Cell Mol. Med. 26 (2022) 601–623.
[5] R. Zura, Z. Xiong, T. Einhorn, J.T. Watson, R.F. Ostrum, M.J. Prayson, et al., Epidemiology of fracture nonunion in 18 human bones, JAMA Surg 151 (2016) e162775.
[6] C.L. Ekegren, E.R. Edwards, R. de Steiger, B.J. Gabbe, Incidence, costs and predictors of non-union, delayed union and mal-union following long bone fracture, Int. J. Environ. Res. Publ. Health 15 (2018).
[7] E. Gómez-Barrena, P. Rosset, D. Lozano, J. Stanovici, C. Ermthaller, F. Gerbhard, Bone fracture healing: cell therapy in delayed unions and nonunions, Bone 70 (2015) 93–101.
[8] K.M. Emara, R.A. Diab, A.K. Emara, Recent biological trends in management of fracture non-union, World J Orthop 6 (2015) 623–628.
[9] S.P. Lad, J.H. Bagley, I.O. Karikari, R. Babu, B. Ugiliweneza, M. Kong, et al., Cancer after spinal fusion: the role of bone morphogenetic protein, Neurosurgery 73 (2013) 440–449.
[10] J. Shou, S. Li, W. Shi, S. Zhang, Z. Zeng, Z. Guo, et al., 3WJ RNA nanoparticles-aptamer functionalized exosomes from M2 macrophages target BMSCs to promote the healing of bone fractures, Stem Cells Transl Med 12 (2023) 758–774.
[11] W.W.Y. Yau, P.-O. Rujitanaroj, L. Lam, S.Y. Chew, Directing stem cell fate by controlled RNA interference, Biomaterials 33 (2012) 2608–2628.
[12] K.A. Whitehead, R. Langer, D.G. Anderson, Knocking down barriers: advances in siRNA delivery, Nat. Rev. Drug Discov. 8 (2009) 129–138.
[13] O. Levy, E. Ruvinov, T. Reem, Y. Granot, S. Cohen, Highly efficient osteogenic differentiation of human mesenchymal stem cells by eradication of STAT3 signaling, Int. J. Biochem. Cell Biol. 42 (2010) 1823–1830.
[14] S. Khormaee, Y. Choi, M.J. Shen, B. Xu, H. Wu, G.L. Griffiths, et al., Endosomolytic anionic polymer for the cytoplasmic delivery of siRNAs in localized in vivo applications, Adv. Funct. Mater. 23 (2013).
[15] A. Wittrup, J. Lieberman, Knocking down disease: a progress report on siRNA therapeutics, Nat. Rev. Genet. 16 (2015) 543–552.
[16] H. Jafari, P. Ghaffari-Bohlouli, S.V. Niknezhad, A. Abedi, Z. Izadifar, R. Mohammadinejad, et al., Tannic acid: a versatile polyphenol for design of biomedical hydrogels, J. Mater. Chem. B 10 (2022) 5873–5912.
[17] M. Wu, T. Mei, C. Lin, Y. Wang, J. Chen, W. Le, et al., Melanoma cell membrane biomimetic versatile CuS nanoprobes for homologous targeting photoacoustic imaging and photothermal chemotherapy, ACS Appl. Mater. Interfaces 12 (2020) 16031–16039.
[18] Z. Chen, P. Zhao, Z. Luo, M. Zheng, H. Tian, P. Gong, et al., Cancer cell membrane-biomimetic nanoparticles for homologous-targeting dual-modal imaging and photothermal therapy, ACS Nano 10 (2016) 10049–10057.
[19] J.-X. Cai, J.-H. Liu, J.-Y. Wu, Y.-J. Li, X.-H. Qiu, W.-J. Xu, et al., Hybrid cell membrane-functionalized biomimetic nanoparticles for targeted therapy of osteosarcoma, Int. J. Nanomed. 17 (2022) 837–854.
[20] Q. Zhang, M. Xin, S. Yang, Q. Wu, X. Xiang, T. Wang, et al., Silica nanocarrier-mediated intracellular delivery of rapamycin promotes autophagy-mediated M2 macrophage polarization to regulate bone regeneration, Mater today Bio 20 (2023) 100623.
[21] S. Seong, V. Vijayan, J.H. Kim, K. Kim, I. Kim, K. Cherukula, et al., Nano-formulations for bone-specific delivery of siRNA for CrkII silencing-induced regulation of bone formation and resorption to maximize therapeutic potential for bone-related diseases, Biomater. Sci. 11 (2023) 2581–2589.
[22] S. Hosseinpour, M.N. Gomez-Cerezo, Y. Cao, C. Lei, H. Dai, L.J. Walsh, et al., A comparative study of mesoporous silica and mesoporous bioactive glass nanoparticles as non-viral MicroRNA vectors for osteogenesis, Pharmaceutics 14 (2022).

[23] A.R. Sharma, Y.-H. Lee, S.-S. Lee, Recent advancements of miRNAs in the treatment of bone diseases and their delivery potential, Curr Res Pharmacol drug Discov 4 (2023) 100150.
[24] U. Tanaka, S. Kajioka, L.S. Finoti, D.B. Palioto, D.F. Kinane, M.R. Benakanakere, Decitabine inhibits bone resorption in periodontitis by upregulating anti-inflammatory cytokines and suppressing osteoclastogenesis, Biomedicines 9 (2021).
[25] D. Lee, K.-J. Shin, D.W. Kim, K.-A. Yoon, Y.-J. Choi, B.N.R. Lee, et al., CCL4 enhances preosteoclast migration and its receptor CCR5 downregulation by RANKL promotes osteoclastogenesis, Cell Death Dis. 9 (2018) 495.
[26] S. Bernardi, M. Di Girolamo, S. Necozione, M.A. Continenza, T. Cutilli, Antiresorptive drug-related osteonecrosis of the jaws, literature review and 5 years of experience, Musculoskelet Surg 103 (2019) 47–53.